

pubs.acs.org/JACS Article

CO₂ Bubble-Assisted Pt Exposure in PtFeNi Porous Film for High-Performance Zinc-Air Battery

Guanzhi Wang,[†] Jinfa Chang,[†] Supriya Koul, Akihiro Kushima, and Yang Yang*



Cite This: J. Am. Chem. Soc. 2021, 143, 11595-11601



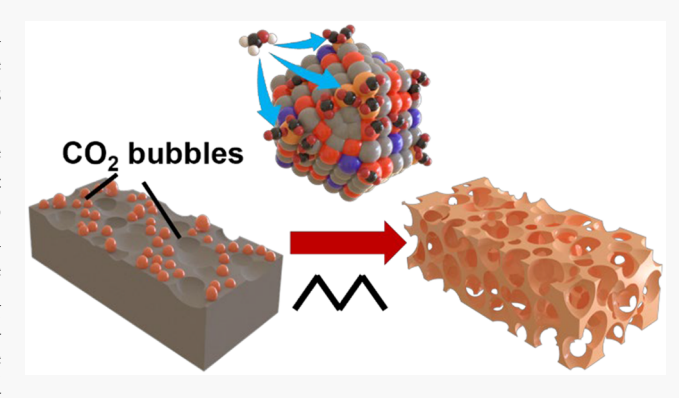
ACCESS

Metrics & More



sı Supporting Information

ABSTRACT: Fine-tuning the exposed active sites of platinum group metal (PGM)-based materials is an efficient way to improve their electrocatalytic performance toward large-scale applications in renewable energy devices such as Zn—air batteries (ZABs). However, traditional synthetic methods trade off durability for the high activity of PGM-based catalysts. Herein, a novel dynamic CO₂-bubble template (DCBT) approach was established to electrochemically fine-tuning the exposed Pt active sites in PtFeNi (PFN) porous films (PFs). Particularly, CO₂ bubbles were intentionally generated as gas-phase templates by methanol electrooxidation. The generation, adsorption, residing, and desorption of CO₂ bubbles on the surface of PFN alloys were explored and controlled by adjusting the frequency of applied



triangular-wave voltage. Thereby, the surface morphology and Pt exposure of PFN PFs were controllably regulated by tuning the surface coverage of CO_2 bubbles. Consequently, the $Pt_{1.1\%}Fe_{8.8\%}Ni$ PF with homogeneous nanoporous structure and sufficiently exposed Pt active sites was obtained, showing preeminent activities with a half-wave potential $(E_{1/2})$ of 0.87 V and onset overpotential (η_{onset}) of 288 mV at 10 mA cm⁻² for oxygen reduction and evolution reactions (ORR and OER), respectively, at an ultralow Pt loading of 0.01 mg cm⁻². When tested in ZABs, a high power density of 175.0 mW cm⁻² and a narrow voltage gap of 0.64 V were achieved for the long cycling tests over 500 h (750 cycles), indicating that the proposed approach can efficiently improve the activity of PGM catalysts by fine-tuning the microstructure without compromising the durability.

■ INTRODUCTION

Developing renewable and efficient energy conversion and storage technologies is urgently needed because of the severe energy crisis and environmental pollution issues. Zinc-air batteries (ZABs) have attracted extensive attention as one of the most promising candidates for next-generation sustainable energy storage systems because of their high theoretical energy density, abundant resources, low cost, and intrinsic safety. However, the sluggish kinetics of multiple electron transfer involving oxygen evolution and reduction reactions (OER and ORR) make ZABs poor in power output performance, hindering their widespread application.3 Because of the optimal electronic structures toward oxygen electrochemical reactions, platinum group metals (PGMs, i.e., Pt, Ir, and Ru)based materials have been studied as efficient ORR/OER electrocatalysts toward high-performance ZABs. The majority of current research is focusing on fine-tuning the exposed active sites of PGMs catalysts through morphology, composition, and surface engineering to achieve high ORR/OER performance at low PGMs loading. 5,6 For instance, blooming efforts have been made on exploring new strategies, such as alloying with low-cost metals, 7,8 surface doping, 9,10 and facet control, 11,12 to improve the utilization efficiency of PGMs. Particularly, alloying Pt with transition metals (PtM, M = Ni,

Fe, Cu, etc.) with low Pt usage has shown great promise to boost ORR activity because of the synergistic contributions of ligand, strain, and ensemble effects induced by the optimized electronic structure. ^{13,14} On the other hand, the rationally used Ni and Fe in the PtM have been proven to exhibit excellent OER performance, enabling the catalysts with supreme bifunctional activities for ZABs. ¹⁵ Nevertheless, traditionally used fine-tuning methods trade off durability for the high activity of PGM-based catalysts, making ZABs have inferior cycling performance. ^{16–18} For instance, Pt-based powdered materials are typically mixed with various carbon supports to enhance the overall surface area and conductivity of ZAB electrodes. ^{19,20} However, carbon supports suffer from severe corrosion issues caused by electrochemical oxidation, leading to severe aggregation/detachment of Pt catalysts and thus rapid degradation of ZAB performance. ¹³ It is crucial to

Received: April 26, 2021 Published: July 16, 2021





develop a highly efficient approach to boost ORR/OER performance by fine-tuning the microstructure of the catalyst without compromising stability. As promising alternatives to powdered materials, conducting PtM porous films (PFs) are expected to exhibit stronger corrosion resistance and unique merits for ZABs, including the highly exposed active sites for electrocatalytic reactions and facilitated mass/ion transport through open channels. 21,22 The PFs are generally fabricated through either top-down etching or bottom-up deposition processes. Among them, dynamic hydrogen bubble template (DHBT) technology is a green and facile method to fabricate metallic PFs, in which the hydrogen (H₂) bubbles act as poreforming agents in situ produced by water electrolysis. 23,24 However, the violent H₂ bubbles generated by the cathodic hydrogen evolution reaction (HER) make it hard to establish a dynamic H2 bubble adsorption/desorption equilibrium in the DHBT-directed electrodeposition process, thus forming disordered and uneven microporous structures.²⁵ Furthermore, the DHBT concept was developed on the basis of the competing reaction between the HER and metal ions electrodeposition (cation electroreduction). Therefore, the applied voltage used in DHBT must be well-controlled to balance HER and the metal deposition. However, when utilizing DHBT to fabricate porous alloy films, it is difficult to adjust the applied potentials to be suitable for all the metal ions deposition and HER simultaneously because of the different reduction potentials of metal ions. Moreover, the different crystal structures and nucleation-growth modes of metals will lead to inhomogeneous morphology and composition of the alloy films formed through DHBT-directed electrodeposition, further increasing the challenge of preparing porous alloy films through the DHBT method.

Inspired by the DHBT-directed metallic PF fabrication process, we herein propose a new concept of using a dynamic CO₂ bubble template (DCBT) for the PF synthesis. The rationale is that carbon dioxide (CO₂) produced from the sluggish and multielectron-transfer-involved methanol electrooxidation reaction (MOR) can be easily controlled and in situ produced as gaseous templates, providing feasible criteria for DCBT-directed synthesis. To verify our hypothesis, we chose Fe-doped PtNi (PFN) PFs as the target platforms and designed an innovative electrochemical DCBT-directed approach for the synthesis of PtM PFs with a controlled nanoporous structure. By introducing in situ MOR into the triangular-wave voltage-driven electrochemical anodization process, CO2 bubbles could constantly form and attach to the PFN film surface, preventing the direct contact between film surface and electrolyte and thus serving as pore-forming agents to produce the homogeneously distributed nanoporous structure. As Pt is the active phase for MOR, the CO₂ bubbles prefer to generate and adsorb on the Pt surface, protecting Pt from oxidation/overetching during the pore-forming process and exposing more Pt active sites. By adjusting triangular-wave frequencies, the dynamic generation, adsorption, residing, and desorption of CO2 bubbles on the PFN film surface can be regulated, leading to the controlled synthesis of nanoporous structure and fine-tuned exposure of Pt active sites. As a consequence, the PFN PFs with nanoporous structure and highly exposed Pt active sites exhibited unparalleled activity and durability when used in ZABs. This new DCBT-directed synthesis method represents a promising avenue for designing low-PGM catalysts for many energy devices beyond ZABs.

RESULTS AND DISCUSSION

The proposed DCBT-directed fabrication of PFN PFs is illustrated in Figure S1, consisting of integrated bottom-up electrodeposition and top-down anodization processes. The PFN alloy was first electrodeposited on stainless steel substrates and then was removed from the substrates to gain the freestanding PFN films, which were subsequently subjected to the DCBT-directed anodization to generate the nanoporous structure. To achieve the proposed DCBT-directed synthesis, we introduced methanol to the anodization electrolyte as a source of CO₂ bubbles. To control the dynamic adsorption/ desorption processes of CO2 bubbles, we first employed square-wave anodization voltages, in which the upper voltage (E_{ij}) is for bubble evolution and the lower voltage (E_{ij}) is for bubble removal. In the square-wave voltage-driven DCBT process, methanol molecules will be first adsorbed on Pt and then dehydrogenized to form adsorbed CO (CO_{ads}) as suggested in Figure 1a.²⁶ However, the CO_{ads} will be adsorbed

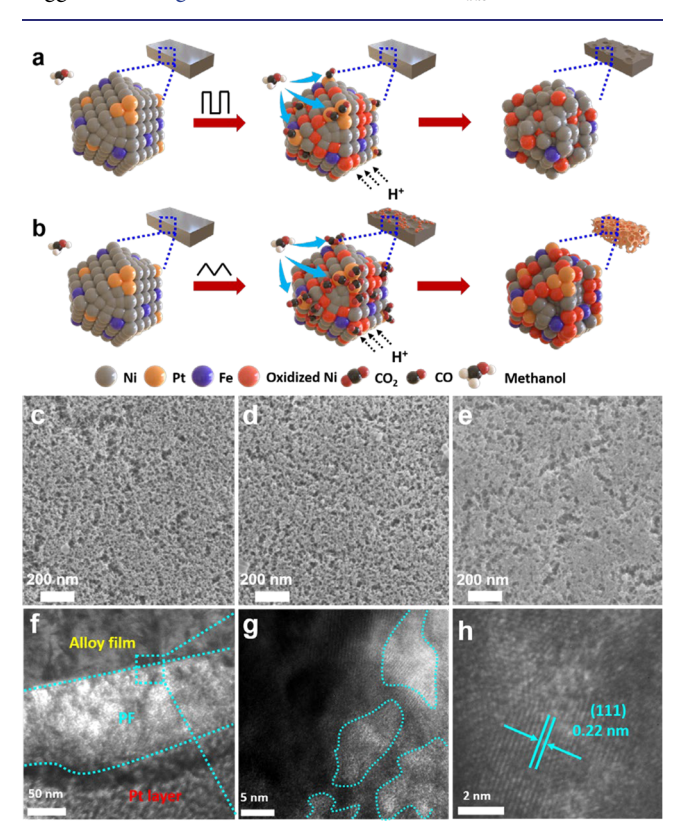


Figure 1. Schematic illustration of DCBT-directed synthesis using (a) square-wave voltage and (b) triangular-wave voltage. SEM images of (c) $Pt_{0.9\%}Fe_{9.0\%}Ni$ PF, (d) $Pt_{1.1\%}Fe_{8.8\%}Ni$ PF, and (e) $Pt_{0.7\%}Fe_{8.1\%}Ni$ PF. (f-h) HR-TEM images of $Pt_{1.1\%}Fe_{8.8\%}Ni$ PF at different magnifications.

strongly on the Pt surface and poison Pt active sites, deteriorating the activity of Pt sites for MOR and thus hindering the complete MOR to CO_2 , which is proved by the rapid decrease in current under constant voltage (Figure S2a).²⁷ As a result, the CO_2 bubbles cannot be generated to construct the DCBT using square-wave voltage, leading to disordered and overetching of metallic Ni in acid solution and failure to form nanoporous structure (Figure 1a). Thereupon, we applied triangular-wave voltage instead of square-wave voltage to address the surface poisoning issue of Pt by CO_{ads} .

effectively setting up a steady-state CO₂ bubbles generation/ detachment equilibrium on the PFN films to implement the DCBT-directed synthesis (Figure 1b). In the triangular-wave voltage mode, the voltage applied on the surface will rise and fall in the mode of symmetrical linear ramp waveform between a given voltage amplitude at a constant frequency, which is similar to the voltage control mode of cyclic voltammetry (CV). Therefore, the working mechanism of the proposed triangular-wave voltage directed anodization process was studied by performing CV tests for MOR within a voltage range of 0.3-2 V (Figure S2b) in a two-electrode cell (i.e., pristine PFN film as the working electrode and Pt mesh as the counter electrode). The voltammogram contains two anodic peaks $(P_{a1} \text{ and } P_{a2})$ and one cathodic peak (P_c) , which is in line with the standard CV curve for MOR using Pt-based materials, indicating that the Pt is the predominant active sites for MOR in the PFN films during the anodization treatment.²⁸ According to the classic MOR mechanism, the dissociative chemisorption of methanol occurs first at low potential around 0.3-0.7 V in the forward scan to form adsorbed species Pt₃COH, along with the formation of adsorbed hydroxyl (OH_{ads}).²⁹ Within the potential range of 0.7-1.5 V, a part of Pt₂CO formed by Pt₃COH dehydrogenation reacts with OH_{ads} to produce CO₂, leaving the unreacted Pt₂CO bonded on Pt to form poisonous Pt=C=O species, corresponding to the first anodic peak P_{al} . Further increasing the voltage to the potential range for OER (above 1.5 V), the surface oxygen species become available and active to react with a part of Pt= C=O, producing CO_2 (P_{a2}). At around 0.72 V (P_c) in the reverse scan, the remaining Pt=C=O will be converted to CO₂ by the re-exposed Pt surface sites after the removal of OH_{ads}. Therefore, in the voltage range sufficient for CO₂ production during the triangular-wave voltage anodization, abundant tiny CO2 bubbles can nucleate and grow at the PFN electrode surface when the concentration of the electrogenerated CO₂ at the electrode surface is sufficiently high (Figure 1b). ^{30,31} To verify the above-discussed mechanism, we analyzed the gas-phase product generated under the control of triangular-wave voltage using the gas chromatograph (GC, Figure S3). The CO₂ peak shown at around 9.5 min was detected from triangular-wave controlled anodization, whereas no CO₂ was detected from square-wave controlled anodization, confirming the significance of using triangular-wave voltage for the DCBT-directed synthesis. In the PFN alloy film with Ni as the dominant component (matrix), the formation of the nanoporous structure depends on the dynamic competitions between surface oxidation, electrochemical etching, and gas bubble coverage. When performing the DCBT-directed synthesis in the acidic electrolyte, the surface Ni was electrochemically oxidized and further dissolved by H+. If CO₂ bubbles were produced and covered on the oxidized Ni surfaces, the direct contact between the oxidized Ni and H+ could be obstructed, leading to decreased etching rate of PFN film. The adsorbed CO2 bubbles could quickly detach from the PFN surface by switching the applied triangular-wave voltages to the potential range without \overline{CO}_2 production, achieving the fine-tuned microstructure of PFN PFs by controlling the dynamic adsorption/desorption of CO2 bubbles on the electrode surface. Significantly, the MOR occurs and produces CO₂ bubbles preferentially on Pt-rich sites in the PFN film, protecting Pt from overetching along with dissolving the oxidized Ni surfaces. Thus, the Pt active sites can be well preserved and exposed by the proposed DCBT-directed

synthesis in a controlled manner. As a result, the dynamically controlled adsorption/desorption of ${\rm CO_2}$ bubbles through adopting an anodization treatment under triangular-wave voltage enables the successful implementation of proposed DCBT-directed synthesis to fabricate PFN PFs with highly ordered nanoporous structure and significantly exposed Pt active sites (Figure 1b).

In the DCBT-directed process, the coverage of CO₂ bubbles on the PFN film surface predominantly determines the microstructure (i.e., pore size and distribution) of the film, which is essentially influenced by the gas generation rate, the bubble residing time on the electrode surface, and the bubble growth rate to reach critical size for detachment.³¹ All these processes are time dependent, suggesting that the frequency adjustment of the triangular-wave voltage can be an appropriate practice in regulating the bubble coverage on the PFN film surface, therefore fine-tuning the microstructure. To validate this concept, we studied triangular-wave voltages with different frequencies (i.e., 10 mHz, 100 mHz, and 1 Hz) in the DCBT-directed treatment to explore the nanopore formation mechanism and realize the controlled synthesis of nanoporous structure. The PFN PFs obtained under different frequencies show ultralow Pt contents (below 1.5 at. %) and very close chemical compositions, which are denoted as Pt_{0.9%}Fe_{9.0%}Ni (at 10 mHz), Pt_{1.1%}Fe_{8.8%}Ni (at 100 mHz), and Pt_{0.7%}Fe_{8.1%}Ni (at 1 Hz), respectively. Note that the subscripts below Pt and Fe are the atomic percentages detected by X-ray fluorescence (XRF, Table S1). X-ray diffraction (XRD, Figure S4) patterns of PFN PFs and pristine PFN alloy film show the same diffraction peaks at 44.5, 51.8, and 76.3°, assigning to the Ni (111), (200), and (220) planes (JCPDS No. 4-0850).² However, the representative diffraction peaks for Pt and Fe were absent in the XRD patterns because of their ultralow contents in the PFN PFs.

The microstructure and surface morphology of PFN PFs were examined by scanning electron microscopy (SEM) to investigate the nanoporous structure formation determined by the dynamic control of CO₂ bubbles. A highly ordered porous structure with homogeneously distributed nanopores sizes of 20-40 nm (thickness of 100 nm, Figure S5) was obtained in the Pt_{0.9%}Fe_{9.0%}Ni PF (Figure 1c). The electrochemical doublelayer capacitance ($C_{\rm dl}$, Figure S6) was also calculated from the CV in the non-Faradaic region to estimate the electrochemically active surface area (ECSA) of PFN PFs. The $Pt_{0.9\%}Fe_{9.0\%}Ni$ PF shows a significantly higher C_{dl} (2.6 mF cm⁻²) than that of pristine PFN alloy film (0.085 mF cm⁻²) without obvious microstructure (Figure S7), confirming the sufficiently exposed active surface in the Pt_{0.9%}Fe_{9.0%}Ni PF. However, the Pt_{0.9%}Fe_{9.0%}Ni PF shows some submicrometer holes formed on the surface (Figure 1c), which is attributed to the overaccumulated time for the generation and growth of CO₂ bubbles at the frequency of 10 mHz, leading to bubble coalescence and detachment from PFN film. When increasing the frequency to 100 mHz, a more homogeneous nanoporous structure with a pore size of about 20 nm and comparable $C_{\rm dl}$ of 2.2 mF cm $^{-2}$ were achieved in the $Pt_{1.1\%}Fe_{8.8\%}Ni$ PF (Figure 1d), indicating the modified accumulated time for the generation and growth of CO2 bubbles. Energy-dispersive Xray (EDX) mapping of Pt_{1.1%}Fe_{8.8%}Ni PF (Figure S8) shows a homogeneous distribution of Ni, Fe, and Pt on the material surface, indicating no phase separation. The slightly higher atomic content of Pt determined by EDX analysis (Table S2) than the result detected from the XRF suggests much higher Pt

exposure on the surface accomplished by the DCBT-directed synthesis. When further increasing the frequency to 1 Hz, a disordered porous structure with irregular large pores was formed in the Pt_{0.7%}Fe_{8.1%}Ni PF (Figure 1e) with a relatively lower $C_{\rm dl}$ of 2.0 mF cm⁻², which may be due to the insufficient protection from CO2 bubbles caused by under-accumulated time for the generation and growth of CO2 bubbles, and the shifted actual potential on the electrode to CO poisoning region resulted from the electrical double layer charge/ discharge at high frequency. Consequently, the PFN film was overetched, forming the heterogeneous porous structure in the Pt_{0.7%}Fe_{8.1%}Ni PF. Note that the above proposed DCBT mechanism at different frequencies is further explained in Figure S9. The PFN PFs obtained from square-wave voltage treatment with different upper potentials (denoted as PFN-LSW and PFN-HSW) also show similar surface morphology (Figure S10) to the Pt_{0.7%}Fe_{8.1%}Ni PF, further implying the failure of square-wave voltage in realizing the DCBT-directed synthesis.

To further examine the morphology and microstructure of Pt_{1.1%}Fe_{8.8%}Ni PF, we executed high-resolution transmission electron microscopy (HR-TEM, Figure 1f, g). A thin lamella was cut from the sample electrode using a focused ion beam (FIB) to analyze the surface. The Pt layer indicated in the figure is a protection layer deposited in the FIB process to prevent ion-beam damages on the specimen surface. A highly porous structure of Pt_{1.1%}Fe_{8.8%}Ni PF with a thickness of 100 nm and pore size of 20 nm was observed, which is consistent with the SEM results. The HR-TEM image of Pt_{1.1%}Fe_{8.8%}Ni PF (Figure 1h) reveals a dominant lattice spacing of ~ 0.22 nm, corresponding to the (111) planes of face-centered cubic (fcc) PtFeNi alloy. 32,33 The TEM-EDX mapping of $Pt_{1.1\%}Fe_{8.8\%}Ni$ PF shows uniform element distribution of Ni, Fe, and Pt, which is consistent with the SEM-EDX mapping results and further verifying no phase separation (Figure S11). X-ray photoelectron spectroscopy (XPS, Figures S12-S14) was also carried out to explore the chemical states of elements in the PFN PFs. All three samples show similar XPS spectra. Only Pt⁰ peaks at 71.2 and 74.6 eV are presented in the XPS Pt 4f spectra (Figures S12-S14a), confirming the metallic phase of Pt in the PFN PFs.³⁴ Similarly, the Ni⁰ (852.6 and 869.9 eV) and Fe⁰ (706.9 and 720.0 eV) peaks were observed in the XPS Ni 2p and Fe 2p spectra (Figures S12-S14b, c), further verifying the metallic phase of the PFN PF. 35,36 Moreover, the oxidation states of Ni (855.8 and 873.3 eV) and Fe (712.5 and 725.6 eV) caused by slight surface hydroxylation were also detected.³⁷ The XPS O 1s spectra of the PFN PFs (Figures S12-S14d) can be assigned to the oxygen from Ni-O and surface adsorbed OHads.

The electrochemical ORR activity of PFN PFs was measured on a rotation ring-disk electrode (RRDE) in a standard three-electrode system. The CV curves of Pt_{1.1%}Fe_{8.8%}Ni PF (Figure 2a) in the O₂- and N₂-saturated 0.1 M KOH aqueous solution were recorded with a sweep rate of 5 mV s⁻¹. Compared with that in the N₂-saturated solution, the CV of Pt_{1.1%}Fe_{8.8%}Ni PF in the O₂-saturated electrolyte exhibits a characteristic cathodic ORR peak at around 0.86 V (vs reversible hydrogen electrode, RHE), demonstrating the prominent ORR activity of Pt_{1.1%}Fe_{8.8%}Ni PF. Figure 2b compares the ORR polarization curves of Pt_{1.1%}Fe_{8.8%}Ni PF with control catalysts at a rotation speed of 1600 rpm and a scan rate of 5 mV s⁻¹ in the O₂-saturated electrolyte. Without DCBT-directed treatment, the PFN alloy film exhibits inferior ORR activity due to the lack of

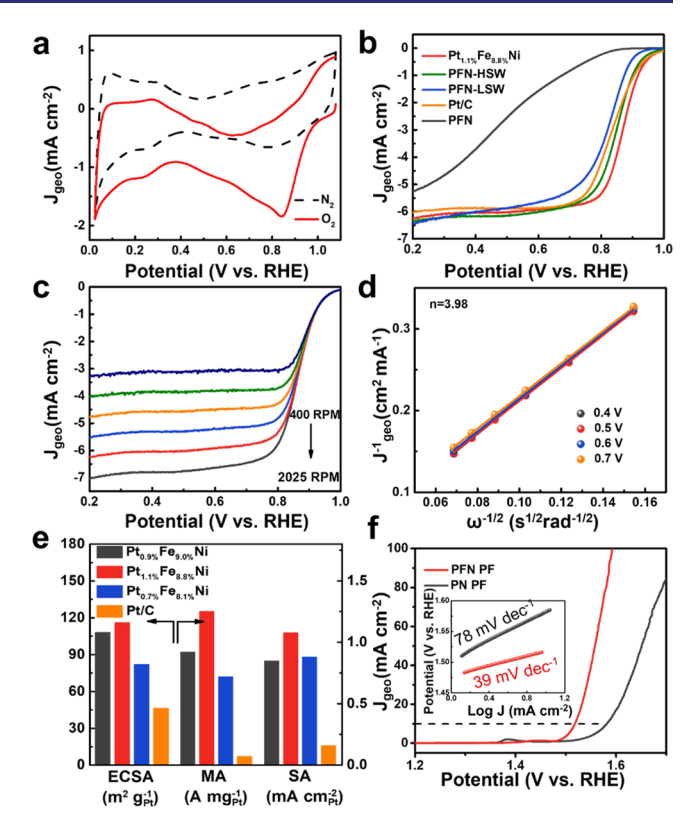


Figure 2. Electrocatalytic ORR and OER performance of PFN PFs. (a) CV curves of $Pt_{1.1\%}Fe_{8.8\%}Ni$ PF measured in the N_2 - and O_2 -saturated 0.1 M KOH electrolytes. (b) ORR polarization curve (without iR-correction) comparison of $Pt_{1.1\%}Fe_{8.8\%}Ni$ PF with other control samples measured at 1600 rpm with a scan rate of 5 mV s⁻¹. (c) ORR polarization curve of $Pt_{1.1\%}Fe_{8.8\%}Ni$ PF recorded at different rotation speeds and (d) the corresponding K-L plots at different potentials. (e) Comparison of $ECSA_{Ptr}$ mass activity (MA), and specific activity (SA) of $Pt_{0.9\%}Fe_{9.0\%}Ni$ PF, $Pt_{1.1\%}Fe_{8.8\%}Ni$ PF, $Pt_{0.7\%}Fe_{8.1\%}Ni$ PF, and commercial Pt/C. (f) OER polarization curve and Tafel plots (inset) of $Pt_{1.1\%}Fe_{8.8\%}Ni$ PF and PtNi PF measured at a scan rate of 5 mV s⁻¹ after 90% iR-correction in 1 M KOH solution.

exposed Pt sites. The Pt_{1.1%}Fe_{8.8%}Ni PF exhibits superior ORR performance with an onset potential (E_{onset}) of 1.0 V (vs RHE) and half-wave potential $(E_{1/2})$ of 0.87 V (vs RHE), which are about 20 mV more positive than that of commercial Pt/C (0.85 V vs RHE). While the PFN PFs obtained using the square-wave treatment (i.e., PFN-LSW and PFN-HSW) show mediocre ORR activities with less positive $E_{1/2}$ (0.81 and 0.84 V vs RHE) than that of Pt_{1.1%}Fe_{8.8%}Ni PF, attributing to the insufficient exposure of Pt sites. Tafel plots derived from the ORR polarization curves of Pt_{1.1%}Fe_{8.8%}Ni PF and other control samples are shown in Figure S15. The much smaller Tafel slope (73 mV dec⁻¹) of Pt_{1.1%}Fe_{8.8%}Ni PF than those of PFN-LSW (139 mV dec^{-1}), PFN-HSW (100 mV dec^{-1}), and Pt/C (89 mV dec⁻¹) indicates a facilitated ORR kinetics with abundant Pt active sites. For an insightful understanding of the ORR reaction kinetics and electron-transfer process for the PFN PFs, linear sweep voltammetry (LSV) curves of Pt_{1.1%}Fe_{8.8%}Ni PF were measured at different rotation speeds and analyzed using the derived Koutecky-Levich (K-L) plots (Figure 2c, d), respectively. According to the K-L plots at different potentials, the ORR electron transfer number (n) of Pt_{1.1%}Fe_{8.8%}Ni PF is estimated to be 3.98, illustrating a favored four-electron transfer process. In the meantime, the electron

transfer number, and the produced peroxide percentage $(\chi_{\rm H_2O_2})$ were also examined from the ring-disk currents using RRDE (Figure S16a). The $Pt_{1.1\%}Fe_{8.8\%}Ni$ PF shows n of almost 4.0 and $\chi_{\rm H,O_2}$ of around 5%, double confirming the fourelectron transfer pathway for ORR. Hence, abundant Pt active sites were exposed sufficiently in the nanoporous structures enabled by the DCBT-directed approach using triangular-wave voltage, significantly boosting the ORR activity of PFN PFs. The frequency-dependent effect of triangular-wave voltage on the Pt exposure was explored by analyzing the CV curves of Pt_{0.9%}Fe_{9.0%}Ni PF, Pt_{1.1%}Fe_{8.8%}Ni PF, Pt_{0.7%}Fe_{8.1%}Ni PF, PFN-LSW, and PFN-HSW in the N2-saturated 0.1 M KOH solution (Figure S16b). All the PFN PFs present well-defined characteristic CV curves for Pt (i.e., hydrogen under-potential adsorption/desorption (H_{upa/upd}) peaks and oxidation/reduction peaks). The ECSA_{Pt} of PFN PFs were then calculated by integrating the H_{upd} peaks within the potential range of 0.05-0.4 V (vs RHE) in the CV curves and compared in Figure 2e. The Pt_{1.1%}Fe_{8.8%}Ni PF displays an outstanding ECSA_{Pt} of 116.3 m² g⁻¹ Pt, which is much higher than those of commercial Pt/ C (46.5 $\text{m}^2\ \text{g}^{-1}\ \text{Pt}$), $Pt_{0.9\%}Fe_{9.0\%}Ni\ (108.1\ \text{m}^2\ \text{g}^{-1}\ \text{Pt}$), $Pt_{0.7\%}Fe_{8.1\%}Ni\ (82.0\ \text{m}^2\ \text{g}^{-1}\ \text{Pt}$) PFs, PFN-LSW (92.6 $\text{m}^2\ \text{g}^{-1}$ Pt), and PFN-HSW (96.1 m² g⁻¹ Pt), indicating the most efficiently exposed Pt active sites in the Pt_{1.1%}Fe_{8.8%}Ni PF. Note that the high Pt site area of commercial Pt/C is obtained because of its high Pt loading in the measurements. When normalizing the ORR activities based on the ECSApt, the Pt_{1.1%}Fe_{8.8%}Ni PF possesses a much higher mass activity of 1.25 A mg⁻¹ Pt and specific activity of 1.08 mA cm⁻² Pt than those of $Pt_{0.9\%}Fe_{9.0\%}Ni$ (0.92 A mg^{-1} Pt and 0.85 mA cm^{-2} Pt), $Pt_{0.7\%}Fe_{8.1\%}Ni$ (0.72 A mg^{-1} Pt and 0.88 mA cm^{-2} Pt), PFN-LSW (0.33 A mg⁻¹ Pt and 0.36 mA cm⁻² Pt), PFN-HSW (0.61 A mg $^{-1}$ Pt and 0.63 mA cm $^{-2}$ Pt), and Pt/C (0.07 A mg $^{-1}$ Pt and 0.16 mA cm⁻² Pt), amply confirming that the enhanced ORR activity enabled by sufficiently exposed Pt active sites in the PFN PFs can be achieved by adjusting the applied triangular-wave voltage frequency in the DCBT-directed synthesis (Table S3). The much higher specific activity of Pt_{1.1%}Fe_{8.8%}Ni PF over other control samples should be due to the geometry of the nanoporous structure of Pt_{1.1%}Fe_{8.8%}Ni PF, which is more conducive to ion transport.³

The Fe-doping in the PFN PFs is proposed to improve their OER activities for ZABs, which was verified by comparing the iR-corrected OER polarization curves of Pt_{1.1%}Fe_{8.8%}Ni PF and PtNi (PN) PF without Fe-doping (Figure 2f) at a scan rate of 5 mV s⁻¹ in 1 M KOH solution. The Pt_{1.1%}Fe_{8.8%}Ni PF shows an enormous enhancement in the OER activity after Fe-doping and delivers an OER onset overpotential (η_{onset}) of only 288 mV at a current density of 10 mA cm⁻², which is much lower than that of PN PF (350 mV) and other reported Pt-based OER catalysts (Table S4). Notably, the Pt_{1.1%}Fe_{8.8%}Ni PF only requires an overpotential of 360 mV to reach a current density of 100 mA cm⁻², exhibiting superior OER activity. The Tafel plot of Pt_{1.1%}Fe_{8.8%}Ni PF shows a much smaller slop of 39 mV dec⁻¹ than that of PN PF (78 mV dec⁻¹), indicating accelerated OER kinetics by Fe-doping. In 0.1 M KOH solution, Pt_{1.1%}Fe_{8.8%}Ni PF can also show excellent OER activity with an overpotential of 360 mV at a current density of 10 mA cm⁻² and Tafel slope of 53 mV dec⁻¹, which is much lower than those of PN PF (415 mV and 85 mV dec⁻¹) as shown in Figure S17. Moreover, the Pt_{1.1%}Fe_{8.8%}Ni PF shows excellent durability for both ORR and OER (Figure S18),

exhibiting imperceptible activity decay after 24 h stability tests. XRD and SEM-EDX elemental mapping of Pt_{1.1%}Fe_{8.8%}Ni PF after ORR and OER tests (Figure S19—S21) show the well-maintained structural and compositional integrity after electrochemical tests. According to the XPS spectra in Figure S22, the elements in PFN PF after the ORR test can sustain the original chemical states. After OER tests, the metallic Ni, Fe, and Pt phases in PFN PF are oxidized, which is reasonable under high OER operation potential (Figure S23).

The polished Zn plate anodes and Pt_{1.1%}Fe_{8.8%}Ni PF cathodes were assembled to validate the practical application of PFN PFs in ZABs. To prove the advantages of using PFN PFs over the traditional powdered mixture of commercial Pt/C and RuO₂ (Pt/C+RuO₂) electrodes, the control ZABs tests were performed under the same condition for comparison. As shown in Figure S24a, the ZABs (Pt_{1.1%}Fe_{8.8%}Ni PF) deliver an open circuit potential (OCP) of 1.45 V, which is comparable with that of ZABs (Pt/C+RuO₂) and suggests the promising potential in practical application. Besides, two connected ZABs (Pt_{1.1%}Fe_{8.8%}Ni PF) can offer sufficient power to light up blue and yellow light-emitting diode (Figure S24b, c). The charge/discharge polarization curves (Figure 3a) present a notable

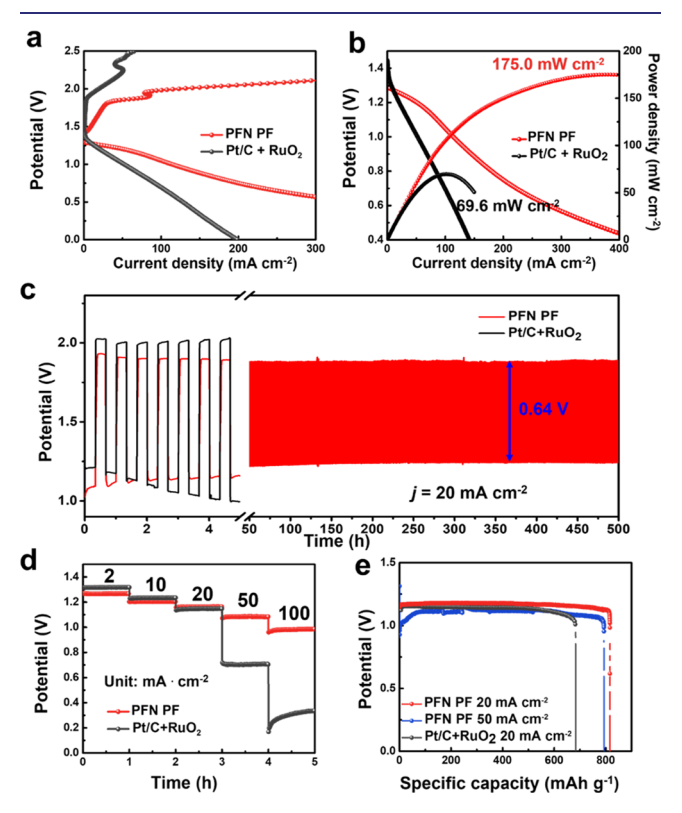


Figure 3. Rechargeable ZABs tests. (a) Charge/discharge polarization curves and (b) power density curves of ZABs assembled using $Pt_{1.1\%}Fe_{8.8\%}Ni$ PF and $Pt/C+RuO_2$. (c) Charge/discharge cycling curves of ZABs ($Pt_{1.1\%}Fe_{8.8\%}Ni$ PF) and ZABs ($Pt/C+RuO_2$) at the current density of 20 mA cm⁻². (d) Discharge curves and (e) specific capacity plots at various current densities.

smaller charge/discharge potential gap of ZABs ($Pt_{1.1\%}Fe_{8.8\%}Ni$ PF) than that of ZABs ($Pt/C+RuO_2$). The ZABs ($Pt_{1.1\%}Fe_{8.8\%}Ni$ PF) deliver a preeminent peak power density of 175.0 mW cm⁻² at the current density of 330 mA cm⁻² (Figure 3b), which is significantly superior to that of ZABs ($Pt/C+RuO_2$) (69.6 mW cm⁻² at 100 mA cm⁻²). The

galvanostatic charge/discharge profiles were measured at a current density of 20 mA cm⁻² to evaluate the rechargeability and cycling stability of ZABs (Figure 3c). The ZABs (Pt_{1.1%}Fe_{8.8%}Ni PF) exhibit an activation process with a gradually reduced potential gap during the initial 100 h and finally maintain an impressive voltage gap of 0.64 V over 400 h. Inversely, the ZABs (Pt/C+RuO₂) show a much larger charge/ discharge voltage gap of 0.82 V and rapid decay within 5 h. Moreover, the ZABs (Pt_{1.1%}Fe_{8.8%}Ni PF) can attain a small voltage gap of 0.71 V at a high current density of 50 mA cm⁻² for 300 h (Figure S24d), exhibiting splendid performance and outstanding durability (Table S5). Besides, the ZABs (Pt_{1.1%}Fe_{8.8%}Ni PF) offer significant advantages over ZABs (Pt/C+RuO₂) in rate performance (Figure 3d), especially under high current density tests, in which the Pt_{1.1%}Fe_{8.8%}Ni PF maintains decent discharge voltages of 1.08 V at 50 mA cm⁻² and 0.98 V at 100 mA cm⁻². Normalized to the weight of the consumed Zn electrode, the specific capacities of ZABs (Pt_{1.1%}Fe_{8.8%}Ni PF) were calculated to be 816 and 793 mAh g⁻¹ at discharge current densities of 20 and 50 mA cm⁻², respectively, corresponding to the energy density of 938.4 and 856.4 Wh kg⁻¹ (Figure 3e). The distinguished merits of high power density/energy densities and outstanding cycling stability convincingly prove the significance of DCBT-directed synthesis in fine-tuning the microstructure and sufficiently exposing active Pt sites for ZABs, which can be applied to the rational design of innovative materials for other energy devices such as electrolyzers, fuel cells, and beyond.

CONCLUSIONS

A transformative DCBT-directed approach was developed to achieve the fine-tuning and controlled exposure of Pt sites in the PtFeNi alloy films by regulating the dynamic generation, adsorption, residing, and desorption processes of CO2 bubbles on the electrode surface under different frequencies of the applied triangular-wave voltages. The CO2 bubbles are preferentially generated on Pt active sites by MOR, serving as protection agents to prevent Pt from overetching and expose abundant Pt active sites in the obtained PFN PFs. The CO₂ bubble coverage on the PFN films can be controlled by adjusting the triangular-wave potential frequency, which regulates the porous morphology of PFN PFs and thus facilitates the efficient exposure of Pt active sites. In consequence, the bifunctional PFN PFs with highly exposed Pt active sites and Fe-doping display preeminent electrocatalytic activity for both ORR and OER. When they serve as the electrocatalyst in ZABs, they show outstanding performance with a maximum power density of 175.0 mW cm⁻² and maintain a stable cycling performance over 500 h. The proposed DCBT-directed synthesis paves a new avenue for designing innovative materials with low-Pt loading and fully exposed Pt sites for energy conversion and storage systems including but not limited to ZABs.

ASSOCIATED CONTENT

Supporting Information

The Supporting Information is available free of charge at https://pubs.acs.org/doi/10.1021/jacs.1c04339.

Experimental section, additional SEM image, XRD, XPS spectra, and electrochemical data (PDF)

AUTHOR INFORMATION

Corresponding Author

Yang Yang — NanoScience Technology Center, Department of Materials Science and Engineering, Department of Chemistry, and Renewable Energy and Chemical Transformation Cluster, University of Central Florida, Orlando, Florida 32826, United States; orcid.org/0000-0002-4410-6021; Email: Yang.Yang@ucf.edu

Authors

Guanzhi Wang — NanoScience Technology Center and Department of Materials Science and Engineering, University of Central Florida, Orlando, Florida 32826, United States Jinfa Chang — NanoScience Technology Center, University of Central Florida, Orlando, Florida 32826, United States; orcid.org/0000-0002-5066-3625

Supriya Koul – Department of Materials Science and Engineering and Advanced Materials Processing and Analysis Center, University of Central Florida, Orlando, Florida 32826, United States

Akihiro Kushima — NanoScience Technology Center, Department of Materials Science and Engineering, and Advanced Materials Processing and Analysis Center, University of Central Florida, Orlando, Florida 32826, United States; orcid.org/0000-0001-5166-4198

Complete contact information is available at: https://pubs.acs.org/10.1021/jacs.1c04339

Author Contributions

[†]G.W. and J.C. contributed equally. The manuscript was written through the contributions of all authors.

Notes

The authors declare no competing financial interest.

ACKNOWLEDGMENTS

This work was supported by the National Science Foundation under Grant CMMI-1851674 (Y.Y). The XPS test was supported by the NSF MRI XPS: ECCS: 1726636, hosted in MCF-AMPAC facility, MSE, CECS, UCF.

REFERENCES

- (1) Li, M.; Bi, X.; Wang, R.; Li, Y.; Jiang, G.; Li, L.; Zhong, C.; Chen, Z.; Lu, J. Relating Catalysis between Fuel Cell and Metal-Air Batteries. *Matter* **2020**, *2*, 32–49.
- (2) Wang, H.-F.; Tang, C.; Zhang, Q. A Review of Precious-Metal-Free Bifunctional Oxygen Electrocatalysts: Rational Design and Applications in Zn-Air Batteries. *Adv. Funct. Mater.* **2018**, 28, 1803329.
- (3) Niu, W.; Yang, Y. Graphitic Carbon Nitride for Electrochemical Energy Conversion and Storage. ACS Energy Lett. **2018**, *3*, 2796–2815.
- (4) Sun, Y.; Huang, B.; Li, Y.; Xing, Y.; Luo, M.; Li, N.; Xia, Z.; Qin, Y.; Su, D.; Wang, L.; Guo, S. Trifunctional Fishbone-like PtCo/Ir Enables High-Performance Zinc-Air Batteries to Drive the Water-Splitting Catalysis. *Chem. Mater.* **2019**, *31*, 8136–8144.
- (5) Lei, H.; Wang, Z.; Yang, F.; Huang, X.; Liu, J.; Liang, Y.; Xie, J.; Javed, M. S.; Lu, X.; Tan, S.; Mai, W. NiFe nanoparticles embedded N-doped carbon nanotubes as high-efficient electrocatalysts for wearable solid-state Zn-air batteries. *Nano Energy* **2020**, *68*, 104293.
- (6) Wang, G.; Aubin, M.; Mehta, A.; Tian, H.; Chang, J.; Kushima, A.; Sohn, Y.; Yang, Y. Stabilization of Sn Anode through Structural Reconstruction of a Cu-Sn Intermetallic Coating Layer. *Adv. Mater.* **2020**, *32*, 2003684.

- (7) Zhao, X.; Xi, C.; Zhang, R.; Song, L.; Wang, C.; Spendelow, J. S.; Frenkel, A. I.; Yang, J.; Xin, H. L.; Sasaki, K. High-Performance Nitrogen-Doped Intermetallic PtNi Catalyst for the Oxygen Reduction Reaction. ACS Catal. 2020, 10, 10637–10645.
- (8) Bao, M.; Amiinu, I. S.; Peng, T.; Li, W.; Liu, S.; Wang, Z.; Pu, Z.; He, D.; Xiong, Y.; Mu, S. Surface Evolution of PtCu Alloy Shell over Pd Nanocrystals Leads to Superior Hydrogen Evolution and Oxygen Reduction Reactions. ACS Energy Lett. 2018, 3, 940–945.
- (9) Tu, W.; Chen, K.; Zhu, L.; Zai, H.; E, B.; Ke, X.; Chen, C.; Sui, M.; Chen, Q.; Li, Y. Tungsten-Doping-Induced Surface Reconstruction of Porous Ternary Pt-Based Alloy Electrocatalyst for Oxygen Reduction. *Adv. Funct. Mater.* **2019**, 29, 1807070.
- (10) Liu, M.; Zhao, Z.; Duan, X.; Huang, Y. Nanoscale Structure Design for High-Performance Pt-Based ORR Catalysts. *Adv. Mater.* **2019**, *31*, 1802234.
- (11) Wang, X.; Figueroa-Cosme, L.; Yang, X.; Luo, M.; Liu, J.; Xie, Z.; Xia, Y. Pt-Based Icosahedral Nanocages: Using a Combination of {111} Facets, Twin Defects, and Ultrathin Walls to Greatly Enhance Their Activity toward Oxygen Reduction. *Nano Lett.* **2016**, *16*, 1467–1471
- (12) Luo, M.; Sun, Y.; Zhang, X.; Qin, Y.; Li, M.; Li, Y.; Li, C.; Yang, Y.; Wang, L.; Gao, P.; Lu, G.; Guo, S. Stable High-Index Faceted Pt Skin on Zigzag-Like PtFe Nanowires Enhances Oxygen Reduction Catalysis. *Adv. Mater.* **2018**, *30*, 1705515.
- (13) Wang, Y. J.; Zhao, N.; Fang, B.; Li, H.; Bi, X. T.; Wang, H. Carbon-supported Pt-based alloy electrocatalysts for the oxygen reduction reaction in polymer electrolyte membrane fuel cells: particle size, shape, and composition manipulation and their impact to activity. *Chem. Rev.* **2015**, *115*, 3433–3467.
- (14) Matin, M. A.; Lee, J.; Kim, G. W.; Park, H.-U.; Cha, B. J.; Shastri, S.; Kim, G.; Kim, Y.-D.; Kwon, Y.-U.; Petkov, V. Morphing Mn_{core}@Pt_{shell} nanoparticles: Effects of core structure on the ORR performance of Pt shell. *Appl. Catal. B: Environ.* **2020**, 267, 118727.
- (15) Wang, C.; Yang, H.; Zhang, Y.; Wang, Q. NiFe Alloy Nanoparticles with hcp Crystal Structure Stimulate Superior Oxygen Evolution Reaction Electrocatalytic Activity. *Angew. Chem., Int. Ed.* **2019**, *58*, 6099–6103.
- (16) Tian, H.; Li, Z.; Feng, G.; Yang, Z.; Fox, D.; Wang, M.; Zhou, H.; Zhai, L.; Kushima, A.; Du, Y.; Feng, Z.; Shan, X.; Yang, Y. Stable, high-performance, dendrite-free, seawater-based aqueous batteries. *Nat. Commun.* **2021**, *12*, 237.
- (17) Li, Z.; Niu, W.; Yang, Z.; Zaman, N.; Samarakoon, W.; Wang, M.; Kara, A.; Lucero, M.; Vyas, M. V.; Cao, H.; Zhou, H.; Sterbinsky, G. E.; Feng, Z.; Du, Y.; Yang, Y. Stabilizing atomic Pt with trapped interstitial F in alloyed PtCo nanosheets for high-performance zinc-air batteries. *Energy Environ. Sci.* **2020**, *13*, 884–895.
- (18) Chang, J.; Wang, G.; Yang, Y. Recent Advances in Electrode design for Rechargeable Zinc-Air Batteries. Small Sci. 2021, 2100044.
- (19) Lin, R.; Cai, X.; Zeng, H.; Yu, Z. Stability of High-Performance Pt-Based Catalysts for Oxygen Reduction Reactions. *Adv. Mater.* **2018**, *30*, 1705332.
- (20) Shao, M.; Chang, Q.; Dodelet, J. P.; Chenitz, R. Recent Advances in Electrocatalysts for Oxygen Reduction Reaction. *Chem. Rev.* **2016**, *116*, 3594–3657.
- (21) Liang, K.; Li, L.; Yang, Y. Inorganic Porous Films for Renewable Energy Storage. ACS Energy Lett. 2017, 2, 373–390.
- (22) Pan, F.; Li, Z.; Yang, Z.; Ma, Q.; Wang, M.; Wang, H.; Olszta, M.; Wang, G.; Feng, Z.; Du, Y.; Yang, Y. Porous FeCo Glassy Alloy as Bifunctional Support for High-Performance Zn-Air Battery. *Adv. Energy Mater.* **2021**, *11*, 2002204.
- (23) Shin, H. C.; Dong, J.; Liu, M. Nanoporous Structures Prepared by an Electrochemical Deposition Process. *Adv. Mater.* **2003**, *15*, 1610–1614.
- (24) Wang, G.; Yang, Z.; Du, Y.; Yang, Y. Programmable Exposure of Pt Active Facets for Efficient Oxygen Reduction. *Angew. Chem., Int. Ed.* **2019**, *58*, 15848–15854.
- (25) Qiu, H. L.; Tang, T. Y.; Asif, M.; Huang, X. X.; Hou, Y. L. 3D Porous Cu Current Collectors Derived by Hydrogen Bubble Dynamic

- Template for Enhanced Li Metal Anode Performance. Adv. Funct. Mater. 2019, 29, 1808468.
- (26) Chung, D. Y.; Lee, K.-J.; Sung, Y.-E. Methanol Electro-Oxidation on the Pt Surface: Revisiting the Cyclic Voltammetry Interpretation. *J. Phys. Chem. C* **2016**, *120*, 9028–9035.
- (27) Cohen, J. L.; Volpe, D. J.; Abruña, H. D. Electrochemical determination of activation energies for methanol oxidation on polycrystalline platinum in acidic and alkaline electrolytes. *Phys. Chem. Chem. Phys.* **2007**, *9*, 49–77.
- (28) Hofstead-Duffy, A. M.; Chen, D.-J.; Sun, S.-G.; Tong, Y. J. Origin of the current peak of negative scan in the cyclic voltammetry of methanol electro-oxidation on Pt-based electrocatalysts: a revisit to the current ratio criterion. *J. Mater. Chem.* **2012**, 22, 5205–5208.
- (29) Mancharan, R.; Goodenough, J. B. Methanol oxidation in acid on ordered NiTi. J. Mater. Chem. 1992, 2, 875–887.
- (30) Ren, H.; Edwards, M. A.; Wang, Y.; White, H. S. Electrochemically Controlled Nucleation of Single CO₂ Nanobubbles via Formate Oxidation at Pt Nanoelectrodes. *J. Phys. Chem. Lett.* **2020**, *11*, 1291–1296.
- (31) Zhao, X.; Ren, H.; Luo, L. Gas Bubbles in Electrochemical Gas Evolution Reactions. *Langmuir* **2019**, *35*, 5392–5408.
- (32) Li, C.; Huang, B.; Luo, M.; Qin, Y.; Sun, Y.; Li, Y.; Yang, Y.; Wu, D.; Li, M.; Guo, S. An efficient ultrathin PtFeNi Nanowire/Ionic liquid conjugate electrocatalyst. *Appl. Catal. B: Environ.* **2019**, 256, 117828.
- (33) Chou, S.-W.; Shyue, J.-J.; Chien, C.-H.; Chen, C.-C.; Chen, Y.-Y.; Chou, P.-T. Surfactant-Directed Synthesis of Ternary Nanostructures: Nanocubes, Polyhedrons, Octahedrons, and Nanowires of PtNiFe. Their Shape-Dependent Oxygen Reduction Activity. *Chem. Mater.* **2012**, *24*, 2527–2533.
- (34) Wang, Y.; Yin, K.; Lv, L.; Kou, T.; Zhang, C.; Zhang, J.; Gao, H.; Zhang, Z. Eutectic-directed self-templating synthesis of PtNi nanoporous nanowires with superior electrocatalytic performance towards the oxygen reduction reaction: experiment and DFT calculation. *J. Mater. Chem. A* **2017**, *5*, 23651–23661.
- (35) Wang, S.; Xiong, L.; Bi, J.; Zhang, X.; Yang, G.; Yang, S. Structural and Electronic Stabilization of PtNi Concave Octahedral Nanoparticles by P Doping for Oxygen Reduction Reaction in Alkaline Electrolytes. ACS Appl. Mater. Interfaces 2018, 10, 27009—27018
- (36) Chen, D.; Zhu, J.; Mu, X.; Cheng, R.; Li, W.; Liu, S.; Pu, Z.; Lin, C.; Mu, S. Nitrogen-Doped carbon coupled FeNi3 intermetallic compound as advanced bifunctional electrocatalyst for OER, ORR and zn-air batteries. *Appl. Catal. B: Environ.* **2020**, 268, 118729.
- (37) Xie, X.; Shang, L.; Shi, R.; Waterhouse, G. I. N.; Zhao, J.; Zhang, T. Tubular assemblies of N-doped carbon nanotubes loaded with NiFe alloy nanoparticles as efficient bifunctional catalysts for rechargeable zinc-air batteries. *Nanoscale* **2020**, *12*, 13129–13136.
- (38) Weidler, N.; Schuch, J.; Knaus, F.; Stenner, P.; Hoch, S.; Maljusch, A.; Schäfer, R.; Kaiser, B.; Jaegermann, W. X-ray Photoelectron Spectroscopic Investigation of Plasma-Enhanced Chemical Vapor Deposited NiO_x, NiO_x(OH)_y, and CoNiO_x(OH)_y: Influence of the Chemical Composition on the Catalytic Activity for the Oxygen Evolution Reaction. *J. Phys. Chem. C* **2017**, *121*, 6455–6463.
- (39) Wu, Y.; Qian, Y.; Niu, B.; Chen, J.; He, X.; Yang, L.; Kong, X. Y.; Zhao, Y.; Lin, X.; Zhou, T.; Jiang, L.; Wen, L. Surface Charge Regulated Asymmetric Ion Transport in Nanoconfined Space. *Small* **2021**, 2101099.